Acta Materialia 141 (2017) 217–229

Contents lists available at ScienceDirect

Acta Materialia

journal homepage: www.elsevier.com/locate/actamat

Full length article

Ultralow thermal conductivity in *n*-type Ge-doped $AgBiSe_2$ thermoelectric materials

Hsin-Jay Wu [a, *], Pai-Chun Wei [b], Hao-Yen Cheng [a], Jie-Ru Deng [a], Yang-Yuan Chen [b]

[a] Department of Materials and Optoelectronic Science, National Sun Yat-sen University, Kaohsiung 80424, Taiwan
[b] Institute of Physics, Academia Sinica, Taipei 11529, Taiwan

ARTICLE INFO

Article history:
Received 22 May 2017
Received in revised form
2 August 2017
Accepted 13 September 2017
Available online 14 September 2017

Keywords:
Thermoelectric material
n-type $AgBiSe_2$
Isothermal section
Bi_2Se_3 nano-precipitate

ABSTRACT

The *n*-type I-V-VI_2 $AgBiSe_2$ features intrinsically low κ due to the anharmonicity of chemical bonds. Experimentally-determined isothermal section guides the starting compositions for the following $AgBiSe_2$-based alloys. Among the undoped alloys, the $Ag_{25}Bi_{25}Se_{50}$ exhibits a highest peak of zT~0.75, and yet the neighboring $Ag_{20}Bi_{27.5}Se_{52.5}$, which involves a Se-rich liquid phase, has a much lower zT~0.3 at 748 K, respectively. With the incorporation of Ge, the $(GeSe)_{0.03}(AgBiSe_2)_{0.97}$ exhibits an ultralow κ~0.3 (W/mK), owing to the formation of Bi_2Se_3 nano-precipitate in the size of 20–40 nm. Additionally, the moiré fringes with a periodicity of 0.25 nm are observed in the Bi_2Se_3 nano-precipitate, implying the presence of local mass fluctuation and superlattice, which could further lead to enhancing phonon scattering and reduced κ. As a result, the ultra-low κ~0.3 (W/mK) boosts the peak of zT up to zT~1.05 in *n*-type $(GeSe)_{0.03}(AgBiSe_2)_{0.97}$, which shows a 140% enhancement compared with that of the undoped $AgBiSe_2$.

1. Introduction

Global need for clean and sustainable energy initiates the vigorous expansion in the development of high-efficiency thermoelectric (TE) materials and modules, which aim for the mid-temperature (400 K-800 K) waste heat recovery via the solid-state Seebeck effect [1–3]. In order to evaluate the performance of thermoelectric materials, a dimensionless thermoelectric figure-of-merit ($zT=(S^2/\kappa\rho)T$) is used, where the S refers to the Seebeck coefficient (i.e., the thermal power), ρ is the electrical resistivity, T stands for the absolute temperature and κ is the thermal conductivity that mainly comprises two contributors from the travelling phonons (κ_L) and the transporting electrons (κ_e), respectively. Accordingly, ideal TE material requires low κ and high power factor ($PF= S^2/\rho$), which could be satisfied once a demonstration of "Phonon-glass electron-crystal (PGEC) [4–6]" can be fulfilled. On the basis of PGEC approach [4–6], the heat conducted by phonon scattering is similar to that in a glass while the electrons remain high mobility as that in a crystal.

The I-V-VI_2 compounds (I=Ag, Cu or alkali metal; V=Sb, Bi; and VI_2=S, Se, Te) are promising mid-temperature TE materials, such as *p*-type $AgSbTe_2$ [7,8] and $AgSbSe_2$ [9], which have been considered as alternatives to the lead chalcogenides. As known, high performance TE modules require successfully integration of high-zTs *p*-type and *n*-type TE materials. Nevertheless, the survey and optimization upon *n*-type TE materials do not proceed as smoothly as that of *p*-type TE materials, presumably due to the challenge in band structure engineering and the difference in the lifetime of thermally-activated charged carriers [10,11]. Most of the above-mentioned I-V-VI_2 compounds belong to *p*-type semiconductors, except for the *n*-type $AgBiSe_2$, which attracts growing attentions in recent years [12–14].

A peak zT value of *n*-type $AgBiSe_2$ is 0.5 at 773 K [12], and it can be further improved to 0.9–1.0 through Nb [12] and Cl [13] doping. The $AgBiSe_2$ crystallizes in a hexagonal structure with space group of $P\bar{3}$ m1 ($a,b = 4.194$ Å, $c = 19.65$ Å), experiences a phase transition to an intermediate rhombohedral phase with space group of $R\bar{3}$ m ($a,b = 4.184$ Å, $c = 19.87$ Å) at ~410 K, and turns into a cubic-phase with space group $Fm\bar{3}$ m ($a,b,c = 5.930$ Å) at ~570 K. In the cubic-phase, the strong anharmonicity in chemical bonds leads to strong phonon-phonon Umklapp scattering, resulting in the intrinsically low κ. It is worth mentioning that Ag and Bi atoms share the same cation site in the cubic phase, i.e., the type of ordering or the change of Ag/Bi ratio could lead to different lattice structure of $AgBiSe_2$, and that could greatly affect the electronic and photonic transport properties.

* Corresponding author.
E-mail address: ssky0211@mail.nsysu.edu.tw (H.-J. Wu).

http://dx.doi.org/10.1016/j.actamat.2017.09.029
1359-6454/

Given that the wavelengths of heat-carrier phonons are varying, effective reduction in κ_L might be achieved by increasing the phonon scattering, as a consequence of introducing various dimensions of defects and precipitates. In comparison to the large-scaled secondary phases or mesoscale grain boundaries that effectively scatter the long-wavelength phonons, the nano-precipitates with feature size less than 100 nm have a significant impact upon the scattering of mid-wavelength phonons [15].

Herein, the correlations between the TE properties and materials' microstructural architectures are systematically investigated. Among the $AgBiSe_2$-based alloys, peak zT value of stoichiometric $Ag_{25}Bi_{25}Se_{50}$ achieves 0.75 at 748 K, which is 375% and 150% higher compared with that of pristine $AgBiSe_2$ (zT~0.3 [13] and zT~0.5 [12]), respectively. Moreover, an ultralow κ of 0.3 (W/mK) is found for the n-type $(GeSe)_{0.03}(AgBiSe_2)_{0.97}$, presumably due to the formation of Bi_2Se_3 nano-precipitate, and that further boosts peak zT value to 1.05 at 748 K.

2. Experimental procedure

2.1. Synthesis

In total of 1 g, pure elements of Ag, Bi and Se (99.99%) were weighed according to the pre-determined compositions as listed in Table 1, and sealed in 7 mm × 9 mm quartz tubes under vacuum atmosphere. Each sample ampoule was homogenized at a temperature above the melting point of the alloy (~1123 K) [16] for 12 h, followed by water-quenching process to suppress the grain growth of low-temperature solidification phases and to maintain the fine-grained microstructure. After completely mixing, the sample ampoule was annealed at 773 K for 45 days, to ensure that the thermal equilibrium was reached. Thermally-equilibrated alloys were then subjected to the following metallographic observation, compositional analysis and crystal structure identification.

For TE properties measurements, six ternary alloys, labelling with alloy #A ($Ag_{25}Bi_{25}Se_{50}$), #B ($Ag_{20}Bi_{30}Se_{50}$), #C ($Ag_{17.5}Bi_{32.5}Se_{50}$), #D ($Ag_{20}Bi_{27.5}Se_{52.5}$), #E ($Ag_{17.5}Bi_{30}Se_{52.5}$) and #F ($Ag_{15}Bi_{30}Se_{55}$), and five quaternary Ge-doped $(GeSe)_x(AgBiSe_2)_{1-x}$ ($x = 0.01, 0.03, 0.0.5, 0.07$ and 0.09) were grown using the Bridgman method. In total of 5 g, alloys were loaded in quartz tubes with inner-diameter of 7 mm, sealed under vacuum and subjected for the Bridgman growth in a furnace consisted of three heating zones. Using a constant downward growth rate of 1 (cm/hr), the sample ampoule moved axially from the high-temperature zone, where the alloy was liquid melt, to the low-temperature zone, where the melt solidified completely. Bridgman-grown alloys were subjected for the following TE properties measurements.

2.2. Characterization

Thermally-equilibrated and Bridgman-grown alloys were mounted in epoxy resin, grinding using a series of SiC papers ranging from #800 to #4000, and polishing using the Al_2O_3 powder with particle sizes of 1.0 μm and 0.3 μm, respectively. A field-emission scanning microscope (FESEM, JEOL6330) equipped with a backscattered electron (BSE) detector was employed for metallographic observation while a wavelength dispersive X-ray spectrometer (WDS, JXR-8900R, JEOL) was used to measure the compositions of equilibrium phases. The crystal structure was identified by using a powder x-ray diffractometer (X-ray powder diffractometer, Bruker D-5000) with Cu Kα target at angles (2θ) of 20–90°. The obtained diffraction patterns were compared with the JCPDS database (Joint Committee on Powder Diffraction Standard).

The #G2 alloy ($GeSe_{0.03}(AgBiSe_2)_{0.97}$) was further analyzed using field-emission transmission electron microscopy (FETEM, FEI E.O Tecnai F20 G2) equipped with EDS. The TEM specimen was prepared by the use of focused ion beam (FIB, FEI Nova 200, Japan) milling. In order to reduce the Ga^+ ion-thinning damage, a Pt layer of 3 μm thicknesses was sputtered on the sample's surface. The ion-thinning specimen was taken out by a glass probe, placed on the carbon coated copper/gold mesh and subjected the following TEM analysis. The microstructures were analyzed utilizing the typical bright-field image mode with 200 KV acceleration electron voltage, and their diffraction patterns were obtained using selected-area diffractions (SAD) mode. Furthermore, high-resolution images were taken at magnifications of 250,000–300,000×.

Table 1
Nominal composition of Ag–Bi–Se ternary alloys equilibrated at 773 K together with their equilibrium phases.

No.	Nominal composition (at%)			phase	Equilibrium Composition (at%)		
	Ag	Bi	Se		Ag	Bi	Se
1	75.0	10.0	15.0	Ag_2Se	65.5	1.9	32.6
				L	57.0	41.5	1.5
				Ag	98.6	1.0	0.4
2	60.0	20.0	20.0	Ag_2Se	68.0	0.0	32.0
				L	44.5	52.6	2.9
3	50.0	30.0	20.0	Ag_2Se	67.3	0.0	32.7
				L	29.5	54.5	16.0
4	50.0	20.0	30.0	Ag_2Se	67.2	0.0	32.8
				L	6.8	68.8	24.4
5	40.0	35.0	25.0	Ag_2Se	65.7	0.1	34.2
				L	6.8	68.8	24.4
6	50.0	15.0	35.0	$AgBiSe_2$	26.4	24.7	48.9
				L	6.8	68.8	24.4
				Ag_2Se	66.6	0.0	33.4
7	45.0	20.0	35.0	Ag_2Se	66.3	0.3	33.4
				L	14.6	60.3	25.1
				$AgBiSe_2$	24.8	25.6	49.6
8	20.0	55.0	25.0	Ag_2Se	66.5	0.0	33.5
				L	12.3	63.8	23.9
				$AgBiSe_2$	25.0	25.4	49.6
9	25.0	40.0	35.0	$AgBiSe_2$	24.8	24.5	50.7
				L	14.0	59.0	27.0
				Ag_2Se	66.5	0.0	33.5
10	30.0	20.0	50.0	Ag_2Se	69.5	2.3	28.2
				$AgBiSe_2$	25.9	25.0	49.1
11	45.0	5.0	50.0	$AgBiSe_2$	25.5	23.5	51.0
				L	0.0	0.1	99.9
				Ag_2Se	66.5	0.0	33.5
12	20.0	20.0	60.0	$AgBiSe_2$	23.6	23.6	52.8
				L	0.6	0.0	99.4
13	15.0	15.0	70.0	$AgBiSe_2$	22.6	32.4	45.0
				L	0.0	0.4	99.6
14	12.5	35.0	52.5	$AgBiSe_2$	21.2	29.6	49.2
				Bi_3Se_4	2.1	45.6	52.3
15	10.0	35.0	55.0	$AgBiSe_2$	15.8	32.2	52.0
				Bi_3Se_4	5.9	38.6	55.5
16	12.5	30.0	57.5	$AgBiSe_2$	20.2	28.9	50.9
				L	1.4	0.4	98.2
				Bi_2Se_3	7.6	39.2	53.2
17	25.0	25.0	50.0	$AgBiSe_2$	25.2	24.4	50.4
18	10.0	40.0	50.0	$AgBiSe_2$	18.7	30.4	50.9
				BiSe	2.7	49.0	48.3
19	5.0	60.0	35.0	$AgBiSe_2$	16.7	34.5	48.8
				L	4.5	65.6	29.9
				BiSe	3.3	46.2	50.5
20	5.0	50.0	45.0	$AgBiSe_2$	16.1	32.3	51.6
				L	3.6	77.8	18.6
				BiSe	4.9	40.0	55.1
21	5.0	55.0	40.0	$AgBiSe_2$	18.8	29.5	51.7
				L	3.0	70.6	26.4
				BiSe	2.0	50.8	47.2
22	12.5	47.5	40.0	$AgBiSe_2$	23.4	26.0	50.6
				L	1.7	77.4	20.9
23	10.0	55.0	35.0	$AgBiSe_2$	21.7	32.8	45.5
				L	2.8	73.1	24.1

2.3. TE property measurement

Three temperature-dependent TE properties (S, ρ and κ) of the Bridgman-grown alloys were evaluated within 300 K–750 K. A commercial instrument ZEM-3 (ULVAC-RIKO, Japan) was used, for measuring the S and ρ simultaneously, under a helium-filled atmosphere. Thermal conductivity (κ) are related to the thermal diffusivity (D), the density (d) and the heat capacity (C_p) via the equation $\kappa = CpDd$. A commercial apparatus LFA467 (Netzsch, German) was used to measure the D, while the d is obtained by the Archimedes method. The heat capacity (C_p) was estimated using the Dulong-Petit equation (C_p = 3R/M), where the R is the gas constant and M refers to the molar mass.

3. Results and discussion

Fig. 1 summarizes the temperature dependence zT for two series of Bridgman-grown alloys within 300 K–750 K: (1) alloy #A ($Ag_{25}Bi_{25}Se_{50}$), #B ($Ag_{20}Bi_{30}Se_{50}$), #C ($Ag_{17.5}Bi_{32.5}Se_{50}$), #D ($Ag_{20}Bi_{27.5}Se_{52.5}$), #E ($Ag_{17.5}Bi_{30}Se_{52.5}$) and #F ($Ag_{15}Bi_{30}Se_{55}$), and (2) the Ge-doped quaternary $(GeSe)_x(AgBiSe_2)_{1-x}$ (x = 0.01, 0.03, 0.05, 0.07 and 0.09), labelling with alloys #G1-#G5, respectively. In general, trends of temperature dependence zTs for both doped and undoped samples are similar, which increase with increasing temperature.

It is worth mentioning that the nominal compositions of alloys #A-#F locate inside or neighboring the $AgBiSe_2$ homogeneity regime, resulting in either single-phase $AgBiSe_2$ or multi-phase features. A peak zT value of alloy #A ($Ag_{25}Bi_{25}Se_{50}$) approaches 0.75 at 748 K, which is 150% and 250% higher than that of the reported values (zT = 0.5 at 773 K [12] and zT = 0.3 at 700 K [13], respectively). In comparison to our Bridgman-grown $AgBiSe_2$, the $AgBiSe_2$ synthesized through the conventionally melt-quenching [12] or through the solid-state reaction [13] show higher electrical resistivity and relative lower power factors that leads to lower zT values. The peak zT value for the solution-synthesized $AgBiSe_2$ even drops to 0.03 at 550 K [14]. Herein, the Bridgman-grown $AgBiSe_2$ gives a lower ρ, presumably due to the high packing density, high crystallinity and less grain boundaries, which benefit from Bridgman crystal growth process.

The discrepancy in peak zT value of $AgBiSe_2$ [12–14] might originate from the complicated phase relations and microstructural fluctuations. For example, peak zT value of alloy #D is ~0.3, and that of alloy #E and #F is ~0.5, respectively. Attentions are especially drawn upon the discontinuity in the temperature dependence of zT in Fig. 1, reflecting the phase transformation from rhombohedral-to-cubic at 570 K. However, the transition from hexagonal to rhombohedral at relatively low-temperature (T~410 K) does not induce significant change upon the temperature dependence of zTs, presumably due to the fact that the occupancies of Ag and Bi atoms are ordering and distinguishable in both hexagonal and rhombohedral crystals [13].

To correlate the TE property with phase stability and microstructure, an isothermal section of ternary Ag–Bi–Se system at 773 K (Fig. 2(a)) is determined by collecting the phase equilibrium information from three constituent binaries [17–19] and various thermally-equilibrated alloys. The nominal compositions and

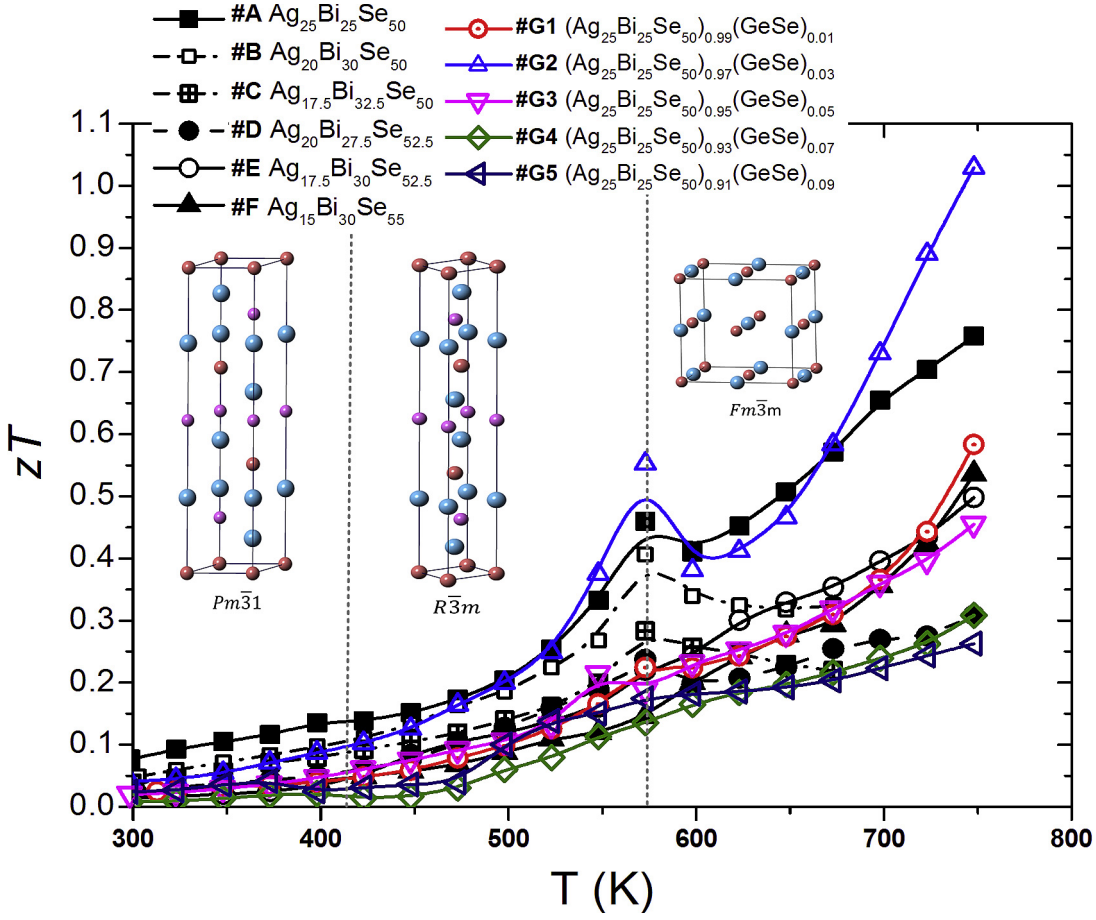

Fig. 1. Temperature dependence of the Bridgman-grown alloys #A-#F and alloys #G1-#G5.

compositions of equilibrium phases are denoted by filled green triangles and open red circles in Fig. 2(a), respectively, and are further summarized in Table 1. The equilibrated microstructures and corresponding XRD patterns of selective alloy #9 (Ag-40.0 at% Bi-35.0 at%Se), alloy#14 (Ag-35.0 at%Bi-52.5 at%Se) and alloy#20 (Ag-50.0 at%Bi-45.0 at%Se) are shown in Fig. 2(b)–(d) and (e)–2(f), respectively, which aim to confirm the phase regions of $AgBiSe_2$+Ag_2Se + liquid, $AgBiSe_2$+Bi_3Se_4, and $AgBiSe_2$+BiSe + liquid. Taking alloy #9 (Fig. 2(b)) as an example, the irregular phases with light-gray and dark-gray contrasts are of $AgBiSe_2$ and Ag_2Se, with compositions of Ag-24.5 at%Bi-50.7 at%Se and Ag-33.5 at%Se, respectively, while the matrix comprises a liquid phase with an average composition of Ag-59.0 at%Bi-27.0 at%Se. Upon quenching, the liquid matrix solidified, and the $AgBiSe_2$ dendrite precipitates out, leaving the remaining matrix as a bright Bi-rich phase.

On the basis of the isothermal section, the solubility of Ag in BiSe and Bi_2Se_3 reaches ~3 at%Ag and ~7 at%Ag, respectively, while the solubility of Bi in Ag_2Se is less significant, which is around ~1 at%Bi. It is worth noting that, due to the similarities in the composition and the crystal structure, it might not be possible to distinguish the Bi_3Se_4 and Bi_4Se_5. In short, the 773 K isothermal section concludes that the ternary $AgBiSe_2$ stabilizes in a homogeneity region of 16.4–26.5 at%Ag and 52.7–45.3 at%Se where it guides the following starting compositions of Bridgman-grown alloys #A-#F.

An enlarged isothermal section superimposed with the starting compositions of the alloys #A-#F is shown in Fig. 3(a), suggesting that alloys #A-#C ($Ag_{25-x}Bi_{25+x}Se_{50}$) locate in the $AgBiSe_2$ single-

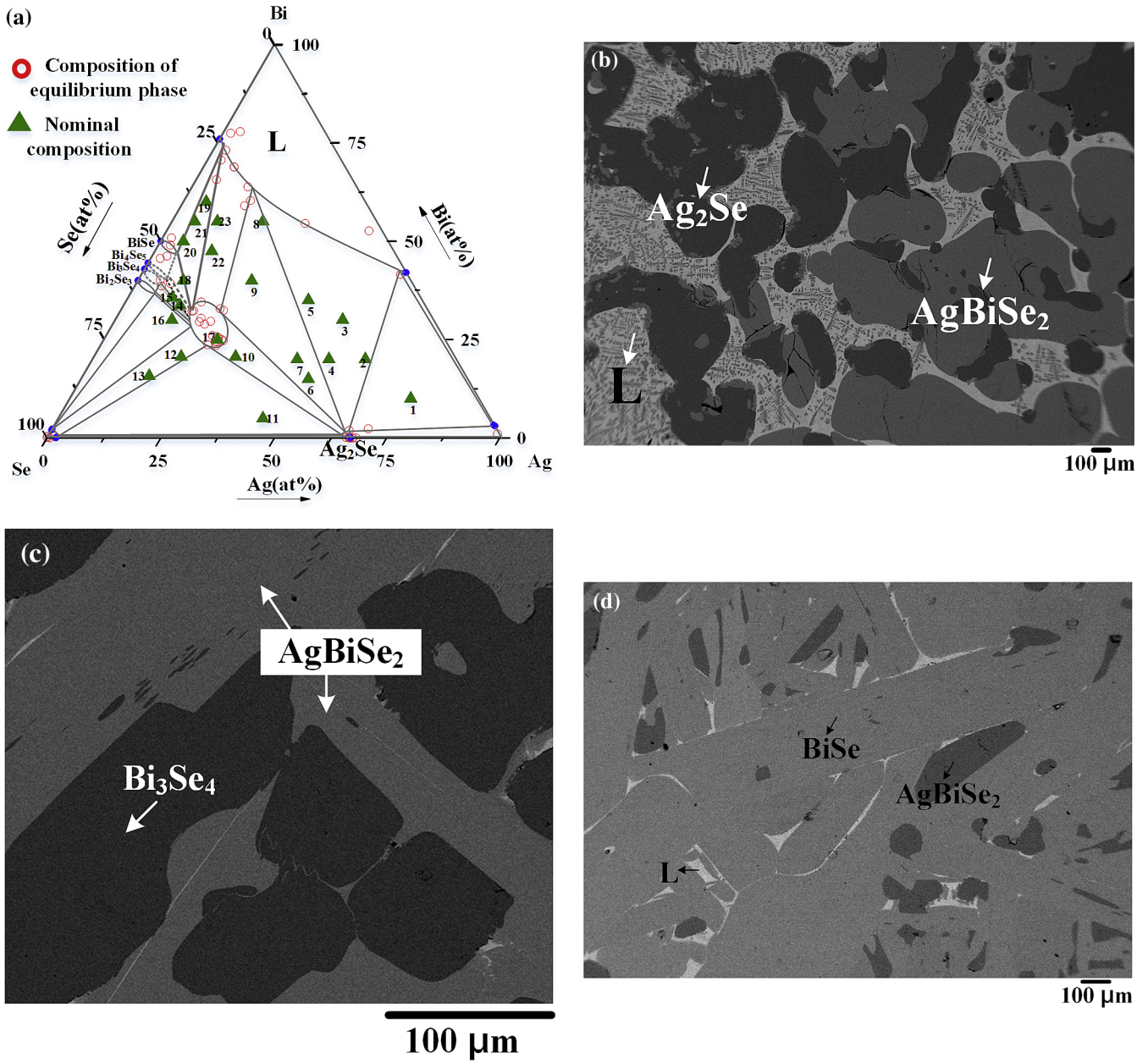

Fig. 2. **(a)** Isothermal section of ternary Ag–Bi–Se system at 773 K superimposed with alloys' nominal compositions. BEI micrographs of Ag–Bi–Se alloys equilibrated at 773 K **(b)** alloy #9 (Ag-40.0 at%Bi-35.0 at%Se), **(c)** alloy#14 (Ag-35.0 at%Bi-52.5 at%Se), **(d)** alloy#20 (Ag-50.0 at%Bi-45.0 at%Se). XRD diffraction pattern of **(e)** alloy #9 (Ag-40.0 at%Bi-35.0 at% Se), **(f)** alloy#14 (Ag-35.0 at%Bi-52.5 at%Se), **(g)** alloy#20 (Ag-50.0 at%Bi-45.0 at%Se).

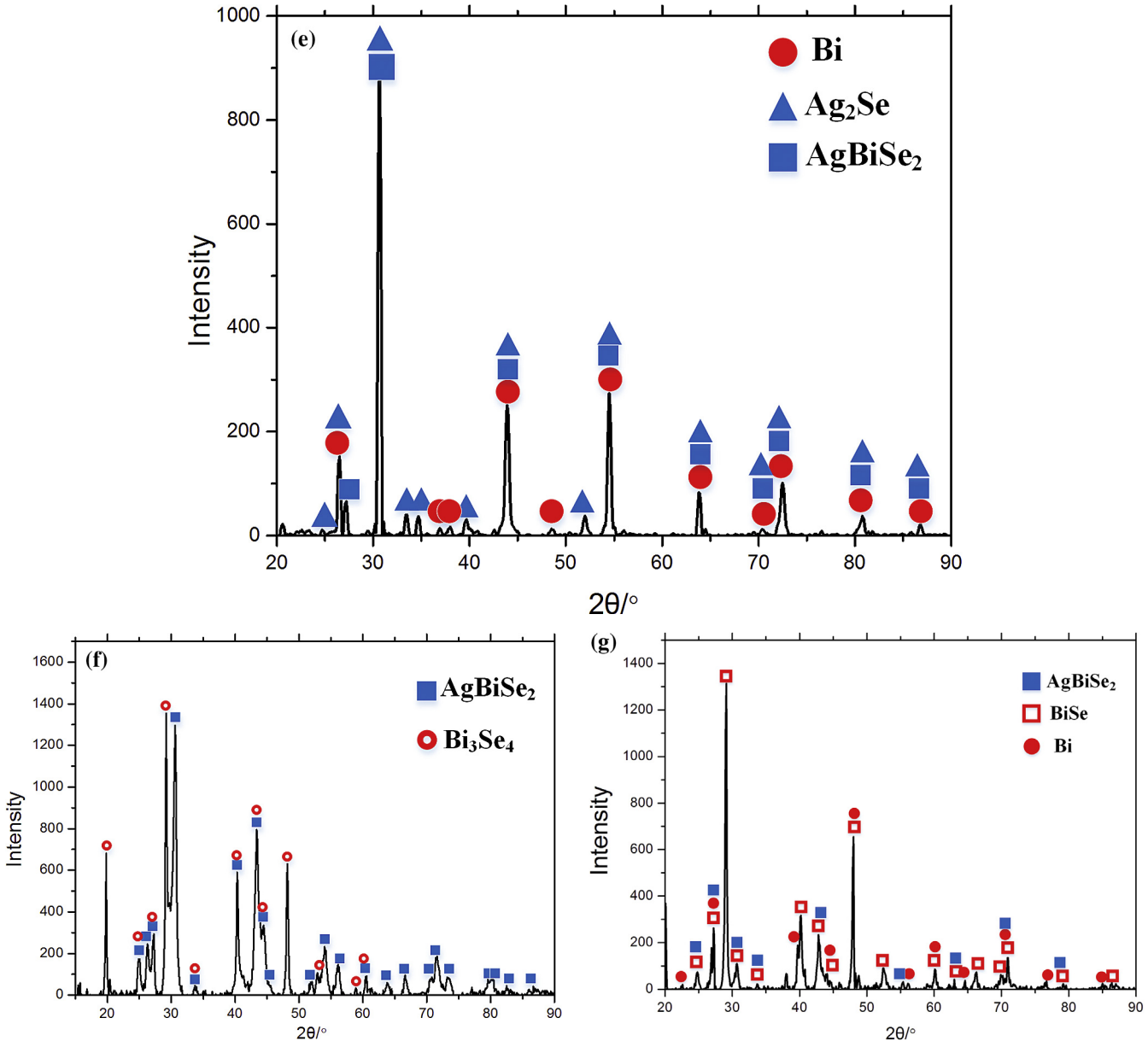

Fig. 2. (*continued*).

phase region, alloy #D ($Ag_{20}Bi_{27.5}Se_{52.5}$) falls in the $AgBiSe_2$+liquid two-phase region, and alloys #E ($Ag_{17.5}Bi_{30}Se_{52.5}$) and #F ($Ag_{15}Bi_{30}Se_{55}$) include the Bi–Se binary compounds (Bi_2Se_3, Bi_3Se_4) in addition to the $AgBiSe_2$, respectively. Fig. 3(b) summarizes the XRD patterns of alloys #A-#F, revealing that the majority phase of all alloys is of $AgBiSe_2$.

Fig. 3(c)–(e) further reveal distinct microstructures in alloy #A, #C and #D. The stoichiometric alloy #A exhibits the polygonal morphology (Fig. 3(c)), while the Bi-enriched alloy #B ($Ag_{17.5}Bi_{32.5}Se_{50}$) stabilizes as a homogeneous solid solution (Fig. 3(d)), respectively. With a slight deviation in the starting composition, the alloy #D ($Ag_{20}Bi_{27.5}Se_{52.5}$) steps outside the $AgBiSe_2$ homogeneity regime (Fig. 3(e)), and incorporates a Se-rich liquid, in addition to the $AgBiSe_2$ matrix. A small inset embedded in Fig. 3(e) gives a clear observation upon the surface morphology of alloy #D, suggesting that the Se-rich liquid reveals rugged surface, due to the fact that the Se could evaporate from the liquid phase during the annealing process. Such a variation in microstructures might lead to the varying peak zT values of alloys #A-#F, which range from the highest zT~0.75 (alloy #A) and the lowest zT~0.3 (alloy #B) at 748 K, respectively.

Fig. 4(a) and (b) show the temperature dependence of S and ρ for alloys #A-#F. The negative values of S suggests that the alloys #A-#F are n-type semiconductors. A discontinuity could also be found in the temperature dependence of S and ρ, which corresponds to the rhombohedral to cubic transformation at T~570 K. Among the three series of alloys ($Ag_{25-x}Bi_{25+x}Se_{50}$, $Ag_{23.75-x}Bi_{23.75+x}Se_{52.5}$ and $Ag_{22.5-x}Bi_{22.5+x}Se_{55}$), the decreasing Ag/Bi ratios degrades the absolute values of S and ρ, presumably implying that the substitution of Ag^+ by Bi^{3+} would increase the carrier concentrations [20]. At 300 K, the value of S range from $S \sim -40$ (μV/K) for alloy #E and #F, to $S \sim -70$ (μV/K) for alloy #A, while the value of ρ are generally low, falling in the range of 2–5 (mΩcm). Within the rhombohedral phase region, the ρ increases with increasing temperature, showing the metallic-like behavior, while the $|S|$ also increases monotonically up to the rhombohedral-cubic transition (T~570 K), where

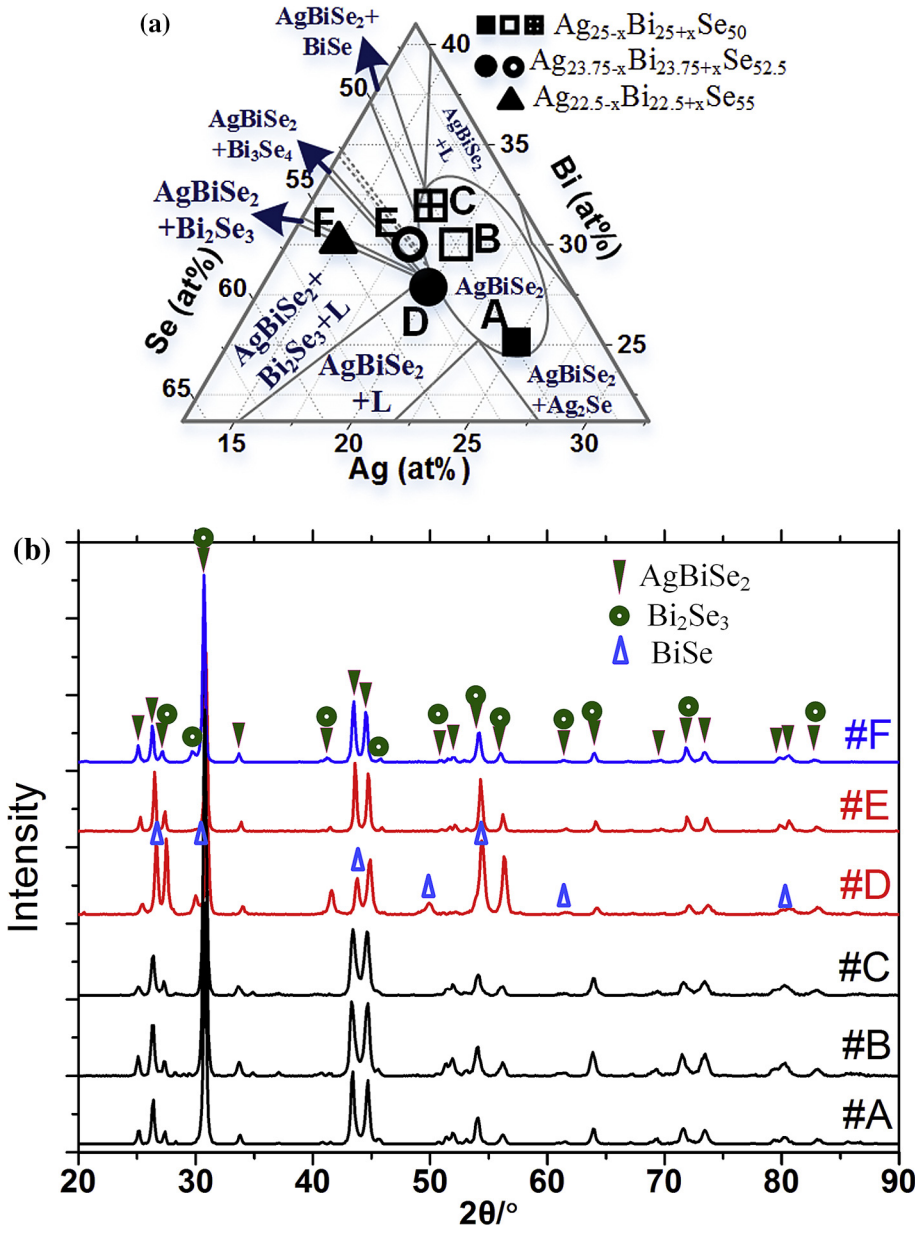

Fig. 3. **(a)** Enlarged isothermal section superimposed with the nominal compositions of Bridgman-grown alloys #A-#F. **(b)** XRD diffraction pattern of Bridgman-grown alloys #A-#F. BEI micrographs of Bridgman-grown **(c)** alloy #A ($Ag_{25}Bi_{25}Se_{50}$), **(d)** alloy #C ($Ag_{17.5}Bi_{32.5}Se_{50}$) and **(e)** alloy #D ($Ag_{20}Bi_{27.5}Se_{52.5}$). A corresponding SEI (secondary electron imaging) image is embedded in Fig. 3(e).

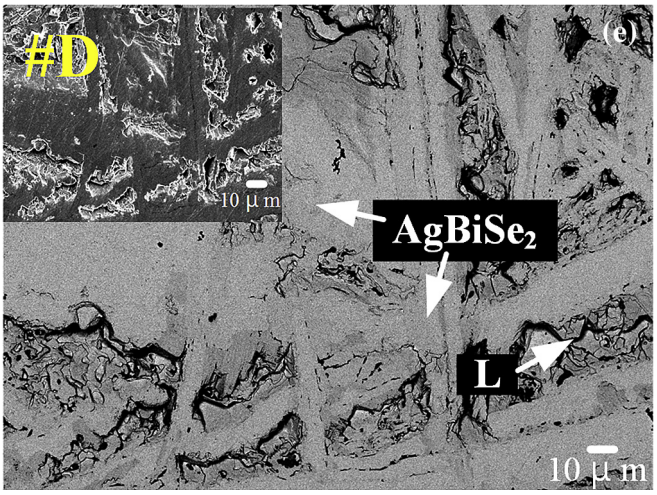

Fig. 3. (*continued*).

the |S| and ρ reach the maximum values. As temperature elevates higher than 570 K, the |S| and ρ drop rapidly and reach a plateau value.

The lattice thermal conductivity κ_L is calculated by $\kappa_L = \kappa - \kappa_e$. The electronic thermal conductivity κ_e can be evaluated using the Wiedemann-Franz law $\kappa_e = LT/\rho$, where L is the Lorentz number.

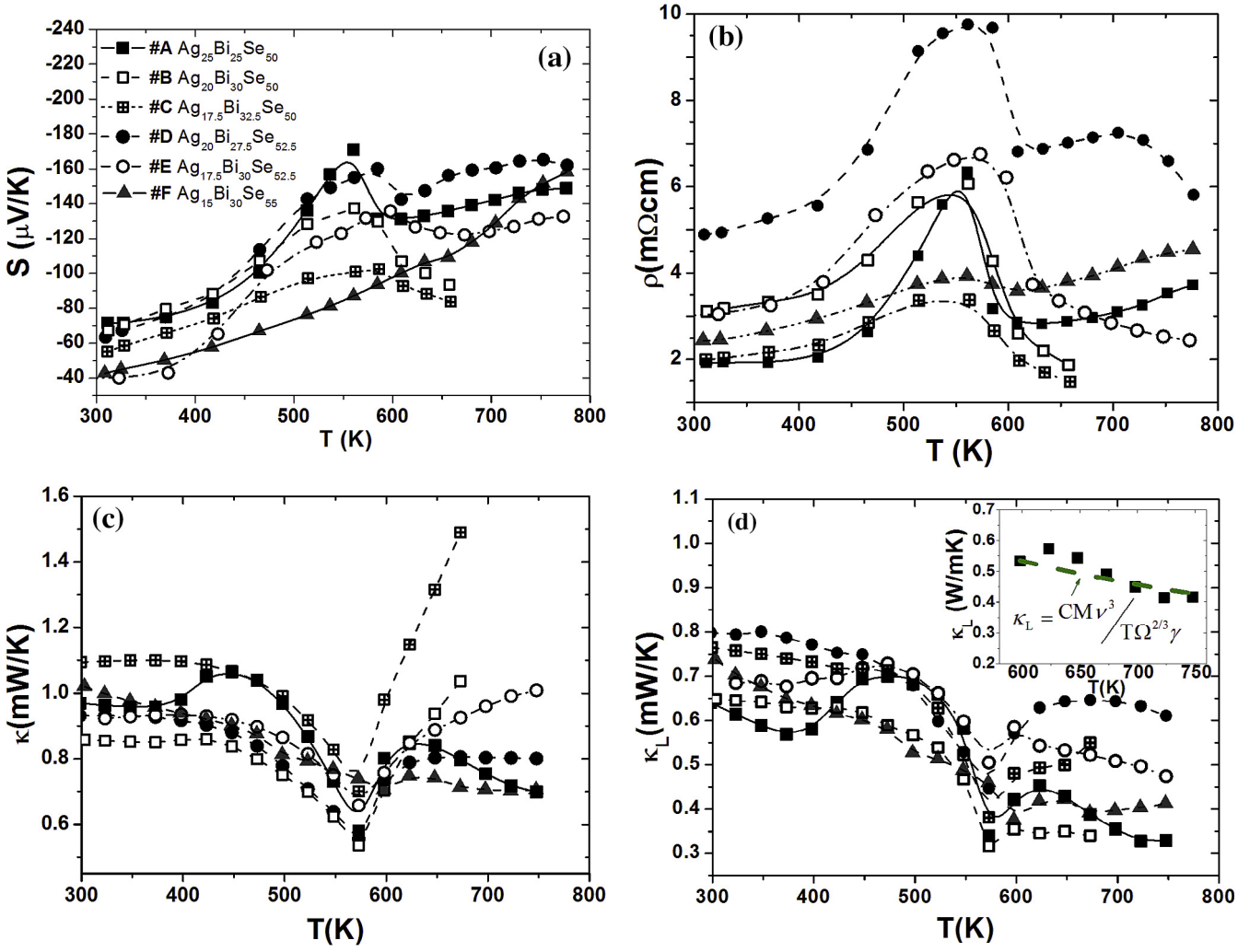

Fig. 4. Temperature dependence of the **(a)** S, **(b)** ρ, **(c)** κ and **(d)** κ_L measured within 300 K–800 K of Bridgman-grown alloys #A-#F.

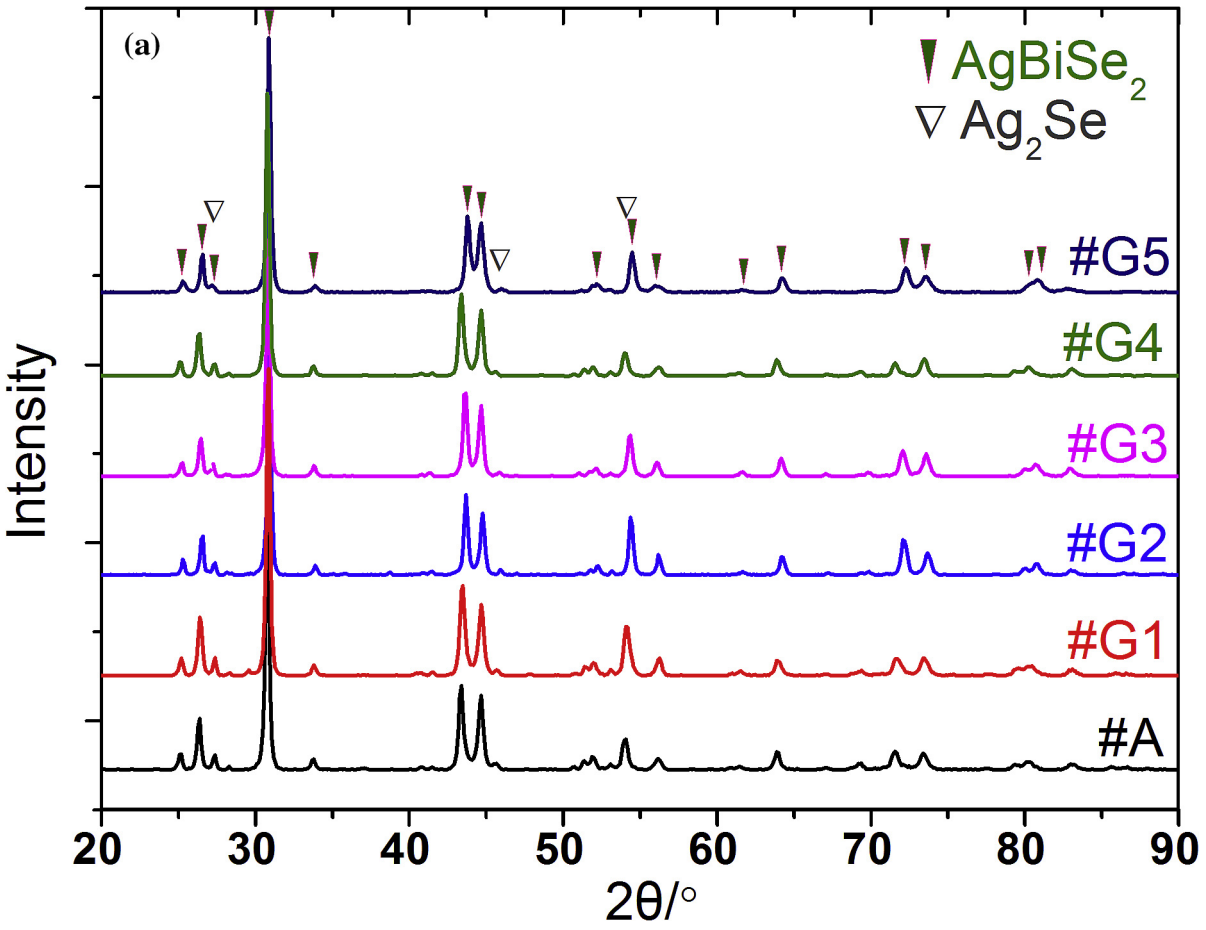

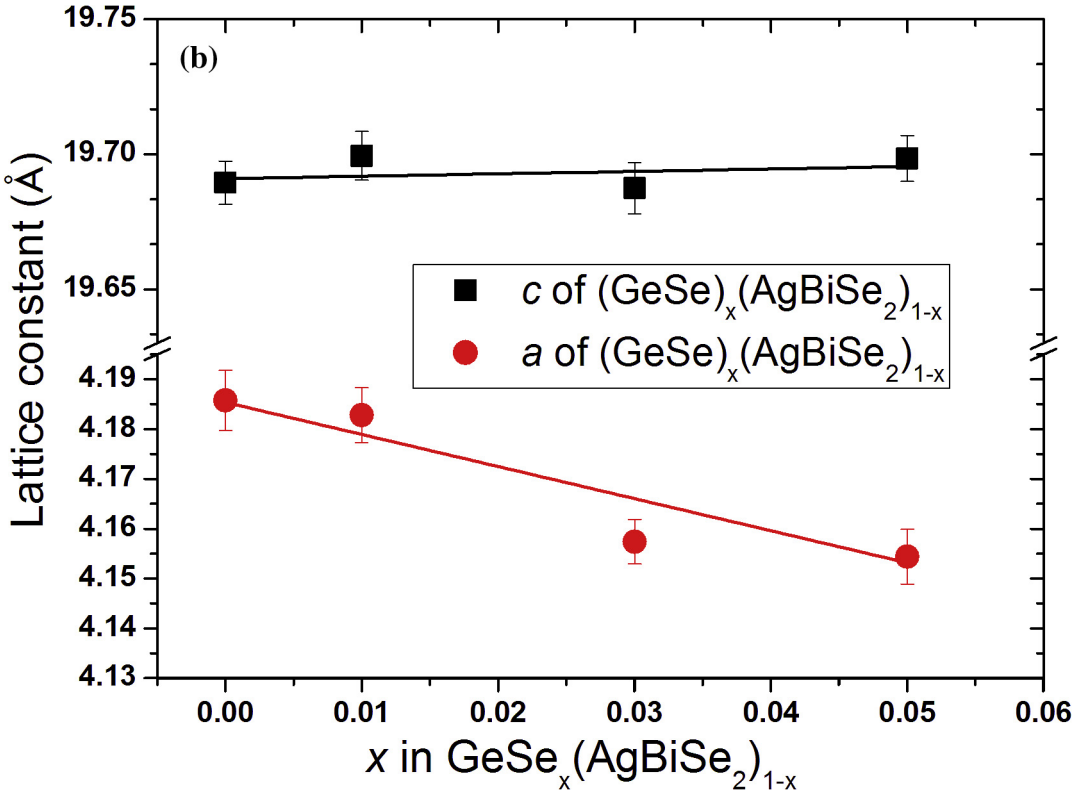

Fig. 5. **(a)** XRD diffraction patterns of alloys #A ($AgBiSe_2$), #G1 ($(GeSe)_{0.01}(AgBiSe_2)_{0.99}$), #G2 ($(GeSe)_{0.03}(AgBiSe_2)_{0.97}$), #G3 ($(GeSe)_{0.05}(AgBiSe_2)_{0.95}$), #G4 ($(GeSe)_{0.07}(AgBiSe_2)_{0.93}$) and #G5 ($(GeSe)_{0.09}(AgBiSe_2)_{0.91}$), **(b)** Lattice constant for alloy #A, #G1, #G2 and #G3. BEI micrographs of the Bridgman-grown **(c)** alloy #G2 and **(d)** alloy #G5.

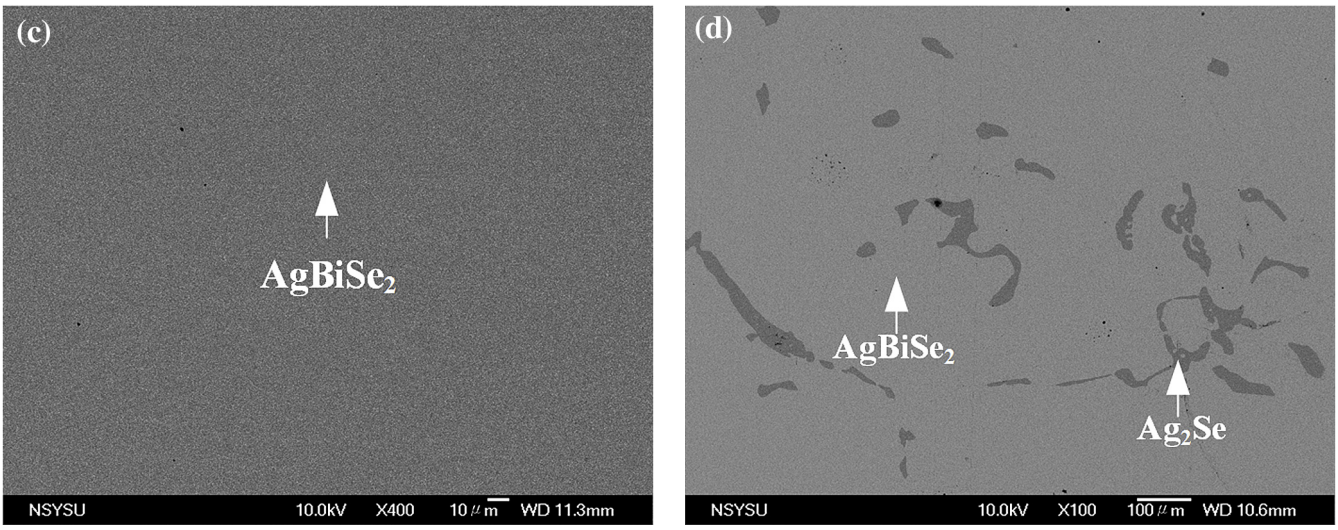

Fig. 5. (*continued*).

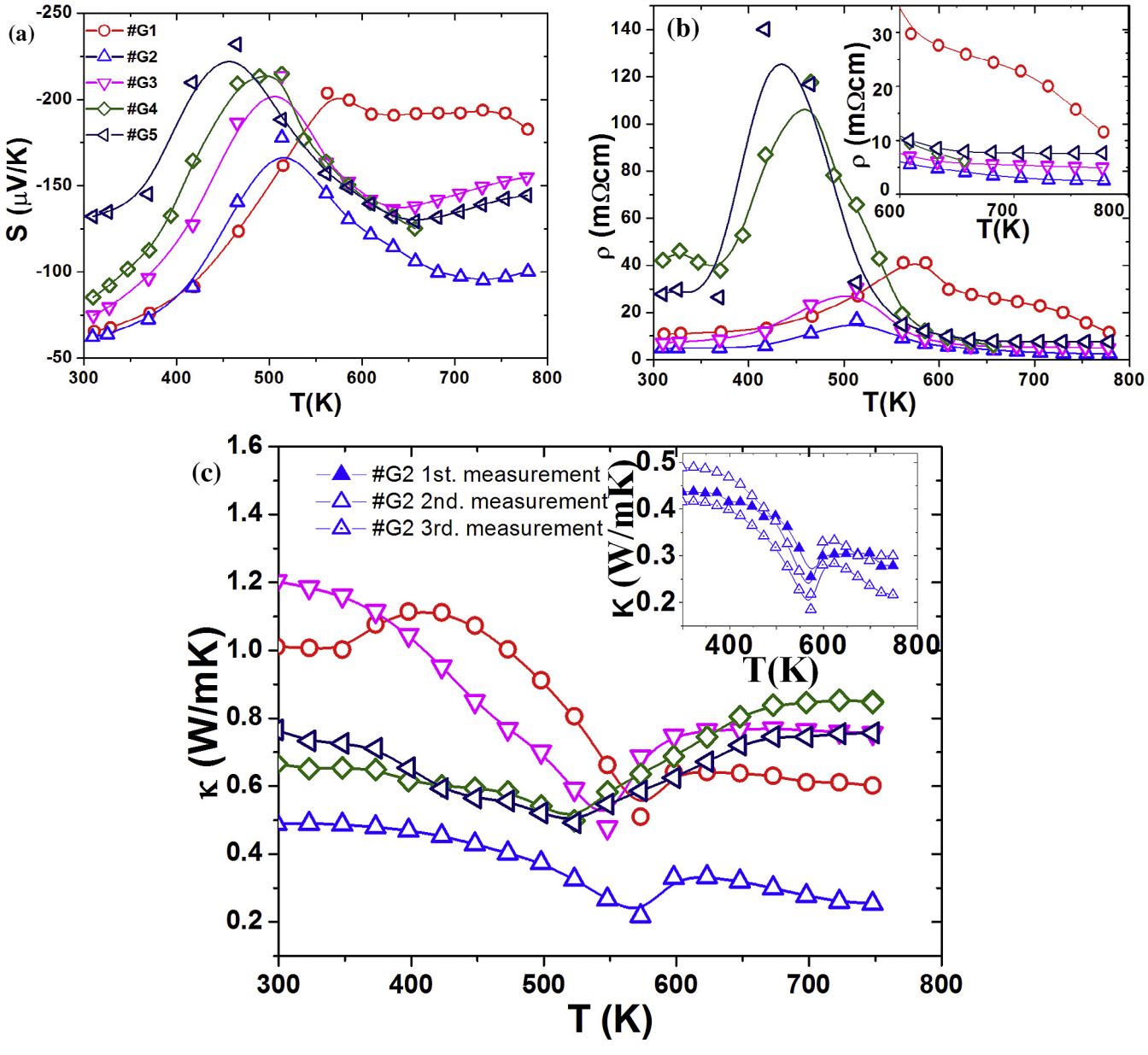

Fig. 6. Temperature dependence of **(a)** S, **(b)** ρ, **(c)** κ and **(d)** κ_L, measured within 300 K–800 K of Bridgman-grown alloys #G1-#G5.

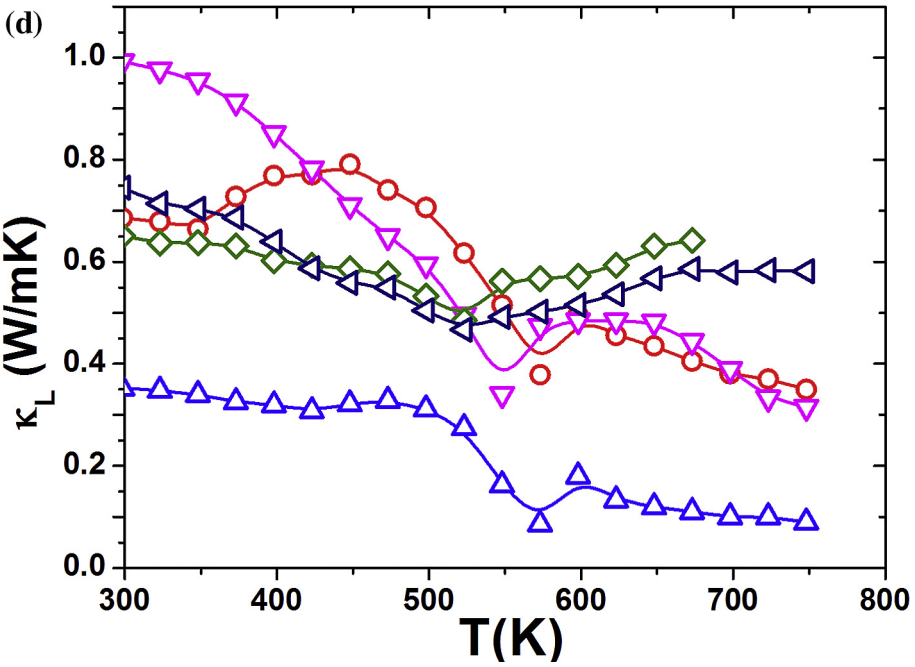

Fig. 6. (*continued*).

The κ and κ_L (Fig. 4(c) and (d)) show a hump near the rhombohedral-cubic phase transition temperature. Among alloy #A-#F, the alloy #A has the lowest κ and κ_L at elevated temperature (κ~0.7 (W/mK) and κ_L~0.4 (W/mK)). One might ascribe the low κ to the high phase-purity of $AgBiSe_2$ with a polygonal morphology (Fig. 3(c)). At 300 K, the κ for alloy #A is 0.96 (W/mK), and remains nearly constant up to ~425 K (at the hexagonal to rhombohedral transition). With further increase in temperature to ~570 K, the κ decreases with increasing temperature. At temperatures higher than 570 K, the κ for alloy #A increases first (~623 K), shows a decrease with increasing temperature, and reached a minimum value of κ~ 0.7 (W/mK) at 748 K. The decrease in κ with respect to the temperature could be attributed to the Umklapp phonon scattering [13]. Mention must be made that the Umklapp phonon scattering is only applicable when κ_e/κ is small. Since the ratio of κ_e/κ is ~0.7 for off-stoichiometric alloy #B and #C, it is therefore only the alloy #A is selected to explain the Umklapp phonon scattering process in $AgBiSe_2$.

Given that the Umklapp phonon scattering dominates the heat conduction for alloy #A, the κ_L is likely to decrease with increasing temperature, following a T^{-1} relation [15]:

$$\kappa_L = C\frac{M\nu^3}{T\Omega^{2/3}\gamma^2} \quad (1)$$

Whereas the C equals to $(6\pi^2)^{2/3}/4\pi^2$ suggested by [21], M is the atomic weight, ν represents the speed of sound, which is assumed to be a constant (~2.28×10^3 m/s), Ω refers to the volume of unit cell and γ is the Grüneisen parameter ($\gamma = 2.05$ for cubic crystal [22]), respectively. As shown in a small inset in Fig. 4(d), the calculated κ_L using Eq. (1), which displays as the green dashed line, fits well with the experimental-obtained κ_L of alloy #A, within 600 K–750 K, implying that the heat conduction of cubic $AgBiSe_2$ fulfills the T^{-1} temperature dependence. As mentioned, the distinct microstructures of alloy #A to #F might be responsible for the varying TE transport properties (i.e. S, ρ and κ), and eventually lead to the fluctuating zTs.

Provided that the alloy #A shows the highest zT, it therefore acts as a starting composition for further incorporating with Ge, to form a series of $GeSe_x(AgBiSe_2)_{1-x}$ (x equals to 0.01, 0.03, 0.05, 0.07 and 0.09), labelled as alloy #G1, #G2, #G3, #G4 and #G5, respectively. The XRD patterns of the $(GeSe)_x(AgBiSe_2)_{1-x}$ are summarized in Fig. 5(a), suggesting that the alloys crystallize from the single-phase $AgBiSe_2$ ($x = 0$–0.05) to the two-phase $AgBiSe_2$+Ag_2Se ($x > 0.05$) with increasing Ge doping. The refined lattice constants (Fig. 5(b)) for single-phase alloys ($x = 0$–0.05 in $(GeSe)_x(AgBiSe_2)_{1-x}$) indicates that a decreases monotonically with increasing x, while c remain almost constant. The shrinkage in the basal plane is contributed from the substitution of the Ag (atomic radius ~1.65 Å) and Bi (atomic radius ~1.43 Å) by the smaller Ge (atomic radius ~1.43 Å). Nevertheless, the anisotropic lattice shrinkage observed in $(GeSe)_x(AgBiSe_2)_{1-x}$, which has also been reported in In-doped Zn_4Sb_3 [23], may not be simply explained by the changes in the covalently bonding lengths or the differences in the ionic radius upon Ge doping. And yet the bonding features and phase transformations in $AgBiSe_2$ might account for the anisotropic structural change. Fig. 5(c) and (d) further demonstrate the difference in microstructures of as-grown alloy #G2 and #G5, which are of single-phase $AgBiSe_2$ and two-phase $AgBiSe_2$+Ag_2Se, respectively.

Fig. 6(a)-(d) summarize the temperature dependence S, ρ, κ and κ_L of alloy #G1-#G5. With the increasing x, the absolute value of maximal S (S_{max}) and and ρ (ρ_{max}) shift to lower temperature, implying that Ge-doping is beneficial to stabilize the high-zT cubic phase. At 300 K, the absolute value of S increase from 60 (μV/K) to 130 (μV/K) as x increases up to 0.09 (i.e., alloy #G5), while the ρ simultaneously show higher values. In Fig. 6(b), the enlarged figure shows the high-temperature ρ of alloy #G1-#G5, which decrease with increasing temperature, while their S increase with increasing temperature, referring the decoupling between S and ρ in the cubic phase.

The κ and κ_L of alloy #G1-#G5 are presented in Fig. 6(c) and (d). As expected, the minimal κ of alloy #G1-#G5 correspond to the rhombohedral-cubic structure transition where the S_{max} and ρ_{max} are also located. Among the Ge-doped and undoped alloys, the alloy #G2 achieves the an extremely low κ~0.3 (W/mK) at 748 K, showing

a significant reduction compared with the undoped alloy #A (κ~0.7 (W/mK)). To validate the reproducibility in κ of alloy#G2, three different measurements are conducted and summarized in an inset in Fig. 6(c), generally giving good consistency. It is also well known that the random occupation of cation atoms in the very same lattice sites is beneficial to reducing the κ/κ_L owing to the enhanced scattering for high-frequency phonons [15].

To further unveil the reason for the ultralow κ_L, the TEM analysis was employed for alloy #G2, which appears to be a homogeneously solid solution (Fig. 5(c)). Unexpectedly, the low-magnification bright-field (BF) image (Fig. 7(a)) suggests that the alloy #G2 exhibits enormous amount of nano-precipitates. The nano-precipitates, as revealed in the high-magnification BF image (Fig. 7(b)), adopt a faceted shape, and the averaged size is about 20–40 nm. An enlarged inverse fast Fourier-Transformation (FFT) view (Fig. 7(c)) indicates excellent crystallinity of the matrix (denoted as R1) and the precipitate (denoted as R2). The chemical compositions of those two regions, analyzed by the EDS (Fig. 7(d)), suggest that the faceted shape R2 phase (the precipitate) is of Bi_2Se_3 while the matrix is of $AgBiSe_2$, with compositions of Ag-37.1 at%Bi-

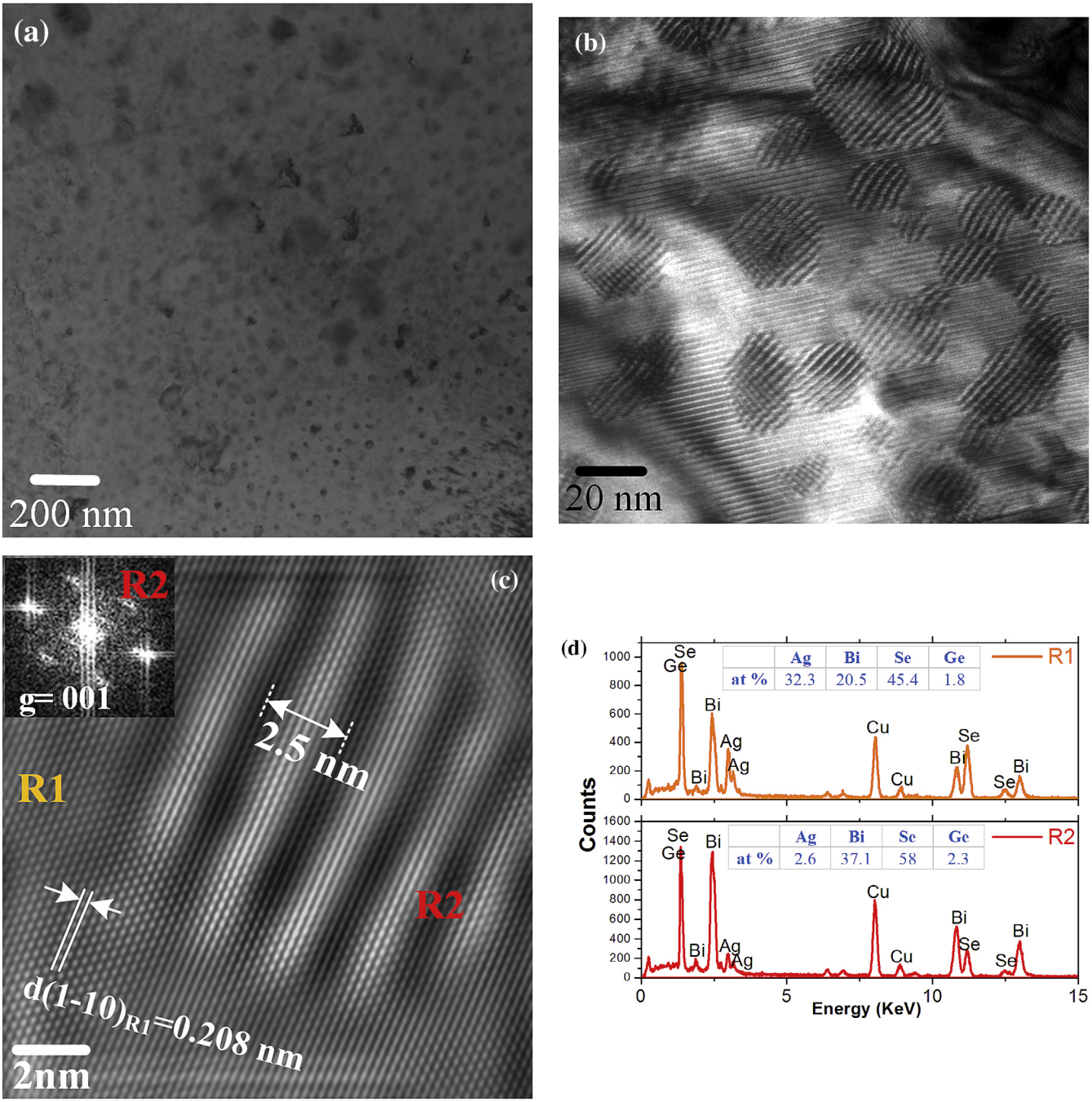

Fig. 7. **(a)** Low magnification and **(b)** high magnification TEM Bright-field images of alloy #G2. **(c)** inverse fast Fourier-Transformation (FFT) image, showing two a nano-precipitate (R2) embedded in the matrix (R1). The FFT image of R2 is embedded in the upper-left corner, suggesting that the $g = 001$. **(d)** the EDS results for matrix (R1) and nano-precipitate (R2). **(e)** the diffraction pattern for figure (a) together with two simulated rhombohedral phases.

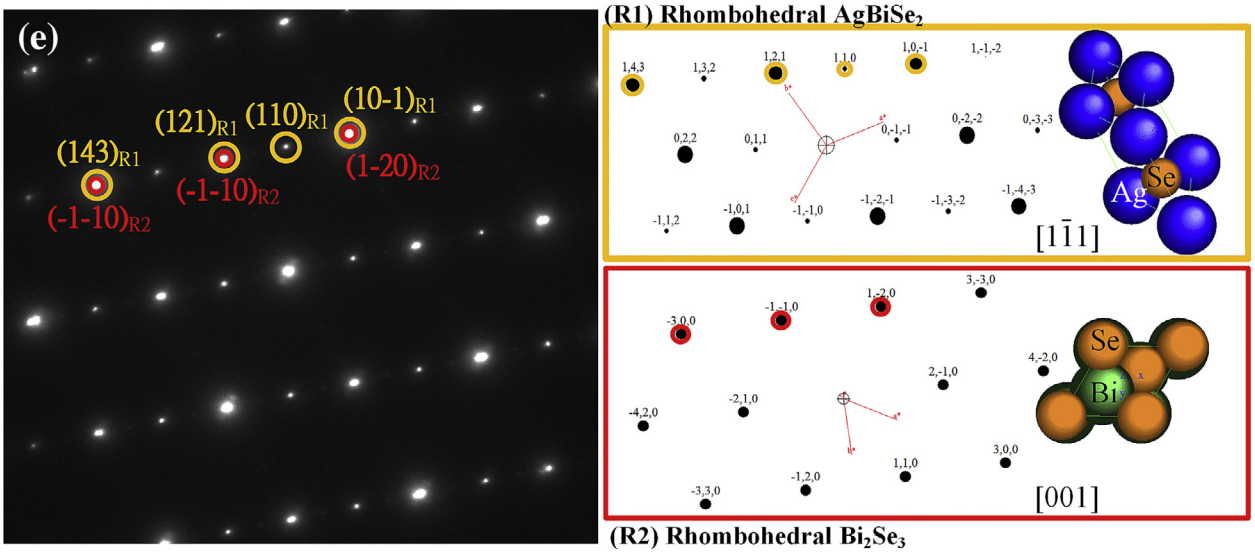

Fig. 7. (*continued*).

58.0 at%Se-2.3 at%Ge and Ag-32.3 at% Bi-45.4 at%Se-1.8 at%Ge, respectively.

Moreover, the typical moiré patterns can be found throughout the R2 phase (Fig. 7(b) and (c)), as shown by the black and white stripes with periodicity of 2.5 nm, which is resulted from the interference of two constituent lattices with nearly the same *d*-spacing. Upon closer observation in Fig. 7 (c), the absence of phase boundary between R1 and R2 indicates the formation of translational moiré fringes that both lattices are nearly parallel. According to Eq. (2), the *d*-spacing for R1 (d_1) and R2 (d_2) phase, under the diffraction condition of $g = 111$ and $g = 001$, respectively, can be related to a set of fringes with spacing d_{tm}:

$$d_2 = \frac{d_{tm} d_1}{(d_1 + d_m)} \tag{2}$$

Given that the d_1 contributed from plane $(10\bar{1})$ is of 0.208 nm and d_{tm} is measured to be 0.25 nm, the calculated d_2 equals to 0.192 nm, which corresponds to the plane (110) in Bi_2Se_3 phase. The observed moiré pattern implies the existence of local mass fluctuations or superlattice, which could enhance the scattering of acoustic phonons [24] so as to significantly reduce the κ. Fig. 7(e) shows the selected area electron diffraction (SAED) pattern of Fig. 7(c), which can be indexed as the coexistence of the $AgBiSe_2$ matrix (R1) and the Bi_2Se_3 precipitates (R2). Both the R1 and R2 phase crystallize in a rhombohedral symmetry ($R\bar{3}m$), but orient along the different zone axis of $[1\bar{1}1]$ and [001], respectively. In short, apart from the intrinsically low κ of $AgBiSe_2$ matrix, the ultralow κ~0.3 (W/mK) of alloy#G2 could be attributed to the combinatorial effects of nano-precipitates and mass fluctuations/superlattice, which are beneficial to the phonon scattering.

4. Conclusions

In summary, the homogeneity regime of $AgBiSe_2$ is depicted by a 773 K isothermal section that collects the phase equilibria information of three constituent binaries and various thermally-equilibrated alloys. Selective *n*-type $AgBiSe_2$-based alloys are grown by the Bridgman method, with the starting compositions spreading near/inside the homogeneity regime of $AgBiSe_2$. Among the undoped alloys, the alloy #A ($Ag_{25}Bi_{25}Se_{50}$) exhibits a peak *zT* value of 0.75 and a moderately low κ~0.7 (W/mK) at 748 K. With properly doping of Ge, an ultralow κ~0.3 (W/mK) is achieved for *n*-type $(GeSe)_{0.03}(AgBiSe_2)_{0.97}$, and that further boosts the peak value of *zT* to 1.05 at 748 K. The TEM analysis of $(GeSe)_{0.03}(AgBiSe_2)_{0.97}$ reveals that the $AgBiSe_2$ matrix is embedded with the faceted shape rhombohedral Bi_2Se_3 precipitates, and forming the translational moiré fringes. The existence of Bi_2Se_3 nano-precipitate with featuring size of 20–40 nm could be beneficial to scattering the acoustic phonons, leading to the reduced κ and enhanced *zT*.

Acknowledgements

The authors acknowledge the financial support of Ministry of Science and Technology of Taiwan (MOST 105-2221-E-110 -022).

References

[1] G. Chen, M.S. Dresselhaus, G. Dresselhaus, J.P. Fleurial, T. Caillat, Recent developments in thermoelectric materials, Int. Mater. Rev. 48 (1) (2003) 45–66.
[2] G.J. Snyder, E.S. Toberer, Complex thermoelectric materials, Nat. Mater. 7 (2008) 105–114.
[3] W. He, G. Zhang, X. Zhang, J. Ji, G. Li, X. Zhao, Recent development and application of thermoelectric generator and cooler, Appl. Energy 143 (2015) 1–25.
[4] G.A. Slack, in: D.M. Rowe (Ed.), CRC Handbook of Thermoelectrics, CRC Press, Boca Raton, FL, 1995, p. 407.
[5] G.S. Nolas, D.T. Morelli, T.M. Tritt, Skutterudites: a phonon-glass-electron crystal approach to advanced thermoelectric energy conversion applications, Annu. Rev. Mater. Sci. 28 (1999) 89–116.
[6] K.B. Sabah, J.P. Fleurial, B.K. Richard, Nanostructured materials for thermoelectric applications, Chem. Commun. 46 (2010) 8311–8324.
[7] H.J. Wu, T.W. Lan, S.W. Chen, Y.Y. Chen, T. Day, G.J. Snyder, State of the art $Ag_{50-x}Sb_xSe_{50-y}Te_y$ alloys: their high zT values, microstructures and related phase equilibria, Acta Mater. 93 (2015) 38–45.
[8] H.-J. Wu, S.-W. Chen, T. Ikeda, G.J. Snyder, Reduced thermal conductivity in Pb-alloyed $AgSbTe_2$ thermoelectric materials, Acta Mater. 60 (2012) 6144–6151.
[9] S.N. Guin, A. Chatterjee, D.S. Negi, R. Datta, K. Biswas, High thermoelectric performance in tellurium free p-type $AgSbSe_2$, Energy Environ. Sci. 6 (2013) 2603–2608.
[10] A.V. Kolobov, On the origin of p-type conductivity in amorphous chalcogenides, J. Non Cryst. Solids 198–200 (1996) 728–731.
[11] N. Tohge, H. Matsuo, T. Minami, Electrical properties of n-type semiconducting chalcogenide glasses in the system Pb-Ge-Se, J. Non-Cryst. Solids 95–96 (1987) 809–816.
[12] L. Pan, D. Berardan, N. Dragoe, High thermoelectric properties of *n*-type $AgBiSe_2$, J. Am. Chem. Soc. 135 (13) (2013) 4914–4917.
[13] S.N. Guin, V. Srihari, K. Biswas, Promising thermoelectric performance in *n*-type $AgBiSe_2$: effect of aliovalent anion doping, J. Mater. Chem. A 3 (2015)

648–655.
[14] C. Xiao, J. Xu, B. Cao, K. Li, M. Kong, Y. Xie, Solid-solutioned homojunction nanoplates with disordered lattice: a promising approach toward "phonon glass electron crystal" thermoelectric materials, J. Am. Chem. Soc. 134 (2012) 7971–7977.
[15] K. Biswas, J. He, I.D. Blum, C.I. Wu, T.P. Hogan, D.N. Seidman, V.P. Dravid, M.G. Kanatzidis, High-performance bulk thermoelectrics with all-scale hierarchical architectures, Nature 489 (2012) 414–418.
[16] Y.M. Shykhyev, Y.A. Yusibov, B.A. Popovkin, M.B. Babanly, The Ag-Bi-Se system, Zh. Neorg. Khim. 48 (2003) 2100–2106.
[17] A.W. Gasior, J. Pstrus, Z. Moser, K. Fitzner, A. Krzyzak, Surface tension and thermodynamic properties of liquid Ag-Bi solutions, J. Phase Equilib. 24 (2003) 40–49.
[18] H. Okamoto, The Bi-Se (Bismuth-Selenium) system, J. Phase Equilib. 15 (1994) 195–201.
[19] I. Karakaya, W.T. Thompson, in: II Ed., in: T.B. Massalski (Ed.), Ag-Se (Silver-Selenium), Binary Alloy Phase Diagrams, vol. 1, 1990, pp. 88–92.
[20] A.F. May, G.J. Snyder, Introduction to modeling thermoelectric transport at high temperature, in: D.M. Rowe (Ed.), Materials, Preparation, and Characterization in Thermoelectrics, vol. 11, CRC Press, Boca Raton, 2012, pp. 1–18.
[21] E.S. Toberer, A. Zevalkink, G.J. Snyder, Phonon engineering through crystal chemistry, J. Mater. Chem. 21 (2011) 15843–15852.
[22] D.T. Morelli, V. Jovovic, J.P. Heremans, Intrinsically minimal thermal conductivity in cubic I-V-VI_2 semiconductors, Phys. Rev. Lett. 101 (2008) 035901–035904.
[23] P.-C. Wei, C.-C. Yang, J.-L. Chen, R. Sankar, C.-L. Chen, C.-H. Hsu, C.-C. Chang, C.-L. Chen, C.-L. Dong, F.-C. Chou, K.-H. Chen, M.-K. Wu, Y.-Y. Chen, Enhancement of thermoelectric figure of merit in β–Zn_4Sb_3 by indium doping control, Appl. Phys. Lett. 107 (2015) 123902–123905.
[24] R. Venkatasubramanian, E. Siivola, T. Colpitts, B. O'Quinn, Thin-film thermoelectric devices with high room-temperature figures of merit, Nature 413 (2001) 597–602.